ACS APPLIED MATERIALS & INTERFACES

www.acsami.org

Research Article

Mesoporous Manganese Oxides with High-Valent Mn Species and Disordered Local Structures for Efficient Oxygen Electrocatalysis

Young Jin Sa,* Sohee Kim, Yesol Lee, Ji Man Kim, and Sang Hoon Joo*

Cite This: *ACS Appl. Mater. Interfaces* 2023, 15, 31393−31402

Read Online

ACCESS | Metrics & More | Article Recommendations | Supporting Information

ABSTRACT: Active and nonprecious-metal bifunctional electrocatalysts for the oxygen reduction reaction (ORR) and oxygen evolution reaction (OER) are vital components of clean energy conversion devices such as regenerative fuel cells and rechargeable metal−air batteries. Porous manganese oxides (MnO_x) are promising electrocatalyst candidates because of their high surface area and the abundance of Mn. MnO_x catalysts exhibit various oxidation states and crystal structures, which critically affect their electrocatalytic activity. These effects remain elusive mainly because the synthesis of oxidation-state-controlled porous MnO_x with similar structural properties is challenging. In this work, four different mesoporous manganese oxides (m-MnO_x) were synthesized and used as model catalysts to investigate the effects of local structures and Mn valence states on the activity toward oxygen electrocatalysis. The following activity trends were observed: m-Mn_2O_3 > m-MnO_2 > m-MnO > m-Mn_3O_4 for the ORR and m-MnO_2 > m-Mn_2O_3 > m-MnO ≈ m-Mn_3O_4 for the OER. These activity trends suggest that high-valent Mn species (Mn(III) and Mn(IV)) with disordered atomic arrangements induced by nanostructuring significantly influence electrocatalysis. In situ X-ray absorption spectroscopy was used to analyze the changes in the oxidation states under the ORR and OER conditions, which showed the surface phase transformation and generation of active species during electrocatalysis.

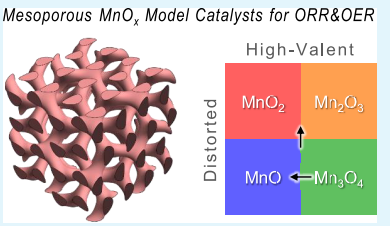

KEYWORDS: *manganese oxide, oxygen evolution, oxygen reduction, electrocatalysis, oxidation state*

INTRODUCTION

The electrocatalytic oxygen reduction reaction (ORR) and oxygen evolution reaction (OER) are universal half-reactions that occur in various energy conversion devices such as fuel cells, electrolyzers, and metal−air batteries.[1−5] The high activation energy of these reactions has necessitated the use of Pt- and Ir-based catalysts to increase the overall performance of such devices.[6,7] Owing to the high cost and limited abundance of the precious metals, the development of earth-abundant metal-based ORR and OER electrocatalysts is vital for the wide application of such energy devices. Nanostructured manganese oxides (MnO_x) have been investigated as promising replacements for state-of-the-art precious-metal-based ORR and OER catalysts[8−15] because Mn is an earth-abundant and environmentally benign element,[16] and nanostructures provide a high surface area which facilitates efficient electrocatalysis.

Understanding the effect of the local structure and oxidation state can facilitate the development of a design strategy for efficient MnO_x-based ORR and OER electrocatalysts.[17−22] According to Mao et al., the ORR activity of MnO_x increases in the following order: MnOOH > Mn_2O_3 > Mn_3O_4 > Mn_5O_8, indicating the critical role of Mn(III) species in ORR.[23] Ticianelli and co-workers reported Mn(III)/Mn(IV) redox-mediated electron transfer to O_2 during the ORR on MnO_x as revealed by in situ X-ray absorption spectroscopy (XAS),[24] while Tang et al. reported that Mn(IV)-rich MnO_x exhibited high ORR activity.[25] The natural oxygen-evolving enzyme in photosystem II with an active center consisting of a calcium manganese oxide ($CaMn_4O_5$) cluster has inspired research in biomimetic Mn-based electrocatalysts.[26−30] $CaMn_xO_y$ compounds with intermediate oxidation states between Mn(III) and Mn(IV) exhibited higher ORR activity.[41] For various MnO_x catalysts, Mn(III) species were found to be responsible for high OER activity.[31−34]

The incorporation of active Mn sites with appropriate oxidation states does not guarantee high electrocatalytic activity. Local structures have been identified as another decisive factor for influencing oxygen electrocatalysis.[35,36] The cubane structure of the natural $CaMn_4O_5$ cluster with the μ_2-oxo-bridged linkage has been mimicked in inorganic MnO_x compounds; the active motif is contained in edge-sharing MnO_6 octahedra.[30] According to Robinson et al., MnO_x catalysts with an edge-sharing MnO_6 geometry and longer Mn−O bonds provided a high photocatalytic activity for water oxidation.[37] Layered birnessites, containing numerous edge-sharing MnO_6, exhibited excellent OER activity,[38−40] and such

Received: March 8, 2023
Accepted: June 20, 2023
Published: June 20, 2023

birnessite-like phase was spectroscopically observed in electrodeposited MnO_x films under OER potentials.[41] Some previous studies focused on the structural flexibility of Mn(III) for high OER activity and stability because $CaMn_4O_5$ clusters contain a slightly distorted cubane structure.[42] However, layered MnO_2 composed of well-ordered edge-sharing MnO_6 are deficient in terminal μ_2-oxo-Mn−O(H) groups; this indicates the importance of disordered atomic arrangements as OER active sites.[43] Consequently, α-MnO_2-based nanocatalysts have been intensively studied because the α-MnO_2 phase contains wide [2 × 2] tunnels (4.6 Å), which facilitate the access of reactants to the μ_2-oxo-Mn−O(H) sites, resulting in high ORR activity. In contrast, the β-MnO_2 phase contains small [1 × 1] tunnels and inactive corner-sharing MnO_6.[44]

To analyze the influence of the Mn oxidation state and local structure of MnO_x catalysts on their catalytic activity, it is vital to synthesize MnO_x model catalysts with similar textural properties. However, this is hampered by the transformation of textural properties and morphologies during oxidation-state and local-structure modulation steps such as heat or chemical treatments. Because the electrocatalytic activity can be significantly influenced by the shape of the catalysts,[45−47] any change in the morphology may complicate activity comparison, leading to improper conclusions. This study describes the preparation of a set of mesoporous MnO_x (*m*-MnO_x) model catalysts by the hard-templating method. Phase transformation occurred inside the solid nanotemplate, inhibiting the structural changes even at high temperatures or under reductive heat treatment. The resulting four types of *m*-MnO_x (MnO_2, Mn_2O_3, Mn_3O_4, and MnO) possessed similar double-gyroid frameworks and textural properties and were used as model electrocatalysts for ORR and OER. Their ORR and OER activity trends indicate that high-valent Mn species (Mn(III) and Mn(IV)) and distorted local structures are the main factors influencing the ORR and OER activity of *m*-MnO_x catalysts. In situ XAS investigations confirmed the generation of the high-valent Mn during electrocatalysis.

EXPERIMENTAL SECTION

Synthesis of *m*-MnO_x. The synthesis of ordered mesoporous silica, KIT-6, was carried out according to a previous report with slight modifications.[48] For the synthesis of *m*-MnO_x,[49] $Mn(NO_3)_2{\cdot}4H_2O$ (8.4 g) in a glass vial was melted at 70 °C for 1 h and added to KIT-6 (6.0 g). The mixture was vigorously agitated and maintained at 100 °C in a closed PP bottle for 13 h. Calcination of the $Mn(NO_3)_x$/KIT-6 composite and removal of the silica template yielded *m*-MnO_x catalysts. Control of the crystal phases of the MnO_x structural frameworks was accomplished by changing the calcination temperature and reduction conditions, as described in detail in the Supporting Information.

X-ray Absorption Spectroscopy. XAS was conducted at the beamline 10C of the Pohang Accelerator Laboratory. For ex situ measurements, the samples and BN powder were mixed thoroughly in a mortar and hand-pelletized in an aluminum holder. In situ XAS measurements were conducted using a homemade spectroelectrochemical cell with a rectangular window. The catalyst-loaded carbon paper was attached to the cell window, with the catalyst side facing the interior of the cell for contact with the electrolyte. The cell contained the electrolyte (0.1 M KOH), an Hg/HgO reference electrode (CHI152, CH Instruments, filled with 1 M KOH), and a graphite rod counter electrode. Initially, the spectrum of a fresh electrode without an applied potential was recorded. Next, the electrode was polarized to 0.6 V (vs reversible hydrogen electrode (RHE)), which is an ORR potential. The electrode was maintained at this potential for 10 min for current stabilization and sufficient phase change and then subject to XAS measurement. Subsequently, XAS spectra were similarly recorded at an OER potential (1.8 V vs RHE). The ARTEMIS software was used for background removal, spectra normalization, and the Fourier transform of the extended X-ray absorption fine structure (EXAFS) spectra.[50]

RESULTS AND DISCUSSION

Physical and Structural Properties of *m*-MnO_x Catalysts. Four *m*-MnO_x model catalysts with controlled oxidation states and local structures were synthesized by the hard-templating method using ordered mesoporous silica (KIT-6) as the template. During synthesis, the oxidation states and local structures of *m*-MnO_x were modified by calcination steps at different temperatures and by the reductive-transformation steps. Thermal treatment generally results in structural deformation that alters structural properties, such as the pore structure and surface area. However, in this study, the silica template maintained the structure of the *m*-MnO_x catalysts during the phase transformation, as confirmed by transmission electron microscopy (TEM) images showing similar pore structures with double-gyroid frameworks regardless of their phases (Figure 1).

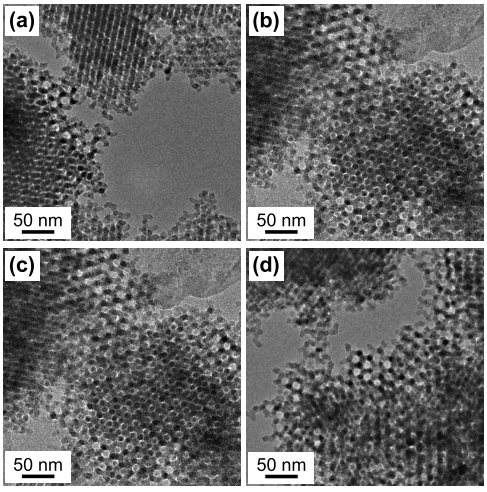

Figure 1. TEM images of (a) *m*-MnO_2, (b) *m*-Mn_2O_3, (c) *m*-Mn_3O_4, and (d) *m*-MnO.

The structural integrity of the catalysts was confirmed by their small-angle X-ray diffraction (XRD) patterns. The XRD patterns of the *m*-MnO_x catalysts showed a main peak at 0.9−1.0° and a shoulder peak at ∼1.1° corresponding to the (211) and (220) reflections of the *Ia*3*d* structure, respectively, similar to the XRD pattern of the KIT-6 template (Figure 2a). Thus, the double-gyroid pore structure of KIT-6 was replicated well in the *m*-MnO_x periodic mesostructures. To identify the crystal phase of the *m*-MnO_x catalysts, their wide-angle XRD patterns were compared with those of bulk-MnO_x reference materials (denoted as b-MnO_x hereafter). The XRD pattern of *m*-MnO_2 was similar to that of b-β-MnO_2; however, in sharp contrast to the spectrum of b-β-MnO_2, the (110) reflection at ∼28.7° in the spectrum of *m*-MnO_2 showed a smaller relative intensity than those of the other peaks (Figure 2b). Notably, the XRD pattern of another MnO_2 polymorph, ε-MnO_2 (akhtenskite), is similar to that of β-MnO_2, except for the peak at 28.7°. There are several polymorphs of MnO_2, each of which exhibits a unique arrangement of MnO_6 octahedral structural units. β-MnO_2 comprises corner-sharing MnO_6 with abundant mono-

https://doi.org/10.1021/acsami.3c03358
ACS Appl. Mater. Interfaces 2023, 15, 31393−31402

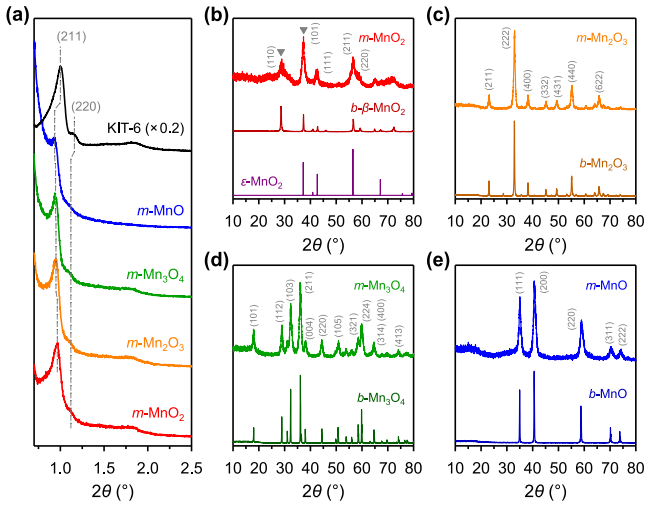

Figure 2. (a) Low-angle XRD patterns of m-MnO_x and the KIT-6 template. High-angle XRD patterns of (b) m-MnO_2, the synthesized b-β-MnO_2 (JCPDS 71-0071), and standard akhtenskite ε-MnO_2 (JCPDS 89-5171) from the database, (c) m-Mn_2O_3 and a commercial b-Mn_2O_3 (JCPDS 24-0508), (d) m-Mn_3O_4 and a commercial b-Mn_3O_4 (JCPDS 18-0803), and (e) m-MnO and commercial b-MnO (JCPDS 78-0424).

μ-oxo bridges, while ε-MnO_2 contains randomly linked MnO_6 octahedra.[51] Hence, m-MnO_2 is composed of β-MnO_2 with partially disordered MnO_6 linkage structures. The XRD peak positions and relative peak intensities of m-Mn_2O_3, m-Mn_3O_4, and m-MnO were consistent with those of the bulk materials, confirming the formation of the corresponding crystal structures (Figure 2b–e). Moreover, the XRD peaks of the m-MnO_x catalysts were broader than those of bulk materials, which is attributed to nanosized crystallites consisting of m-MnO_x with the sizes being ~10 nm calculated by the Scherrer equation (Table S1). Meanwhile, the morphology and particle size of m-MnO_x were analyzed by scanning electron microscopy (Figure S1). The m-MnO_x samples were found to possess irregularly shaped particles with similar sizes of a few microns. For the m-MnO sample, nanowires were observed, which were generated during the H_2 treatment of m-Mn_3O_4, which confirms the importance of the phase transformation occurring inside the mesoporous silica template. However, the number of nanowires in m-MnO was not significant, and the majority of m-MnO particles remained irregular-shaped with double gyroid frameworks. Thus, the particle size and morphology are suggested to have a minimal effect on the electrocatalytic properties.

The textural properties of m-MnO_x were investigated using N_2 adsorption–desorption analyses. The N_2 physisorption isotherms of all the synthesized catalysts showed two hysteresis loops in the relative pressure ranges of 0.45–0.8 and 0.8–0.95 (Figure S2a), which are evidence of the presence of two types of mesopores, as observed in the TEM images (Figure 1). The smaller mesopores originate from the interconnected double-gyroid framework of the two chiral pore channels of the parent KIT-6; occasionally, only one of the two channels is replicated, forming more open structures with larger mesopores. Two types of mesopores were observed in the Barrett–Joyner–Halenda (BJH) pore-size distribution (Figure S2b). A tri-modal pore size distribution was observed, with the peaks at ~3–5, ~12, and ~20 nm, similar to the pore size distributions of previously reported mesoporous metal oxides replicated from KIT-6.[52] All the synthesized catalysts showed similar specific surface areas in the range of 71–104 $m^2\ g^{-1}$ calculated from the Brunauer–Emmett–Teller (BET) equation. Thus, the m-MnO_x catalysts showed similar pore structures, including the surface area, pore volume, and pore size; their detailed textural properties are summarized in Table S1.

The surface chemical states of m-MnO_x were analyzed using X-ray photoelectron spectroscopy (XPS). Two peaks were observed in the Mn 3s spectra, with the lower- and higher-binding energy peaks being the main 3s peak and its satellite peak, respectively. The Mn oxidation states could be qualitatively estimated by comparing the peak splitting between 3s and its satellite peak. For this purpose, the main Mn 3s peak positions were aligned to be 0 eV (Figures 3a and

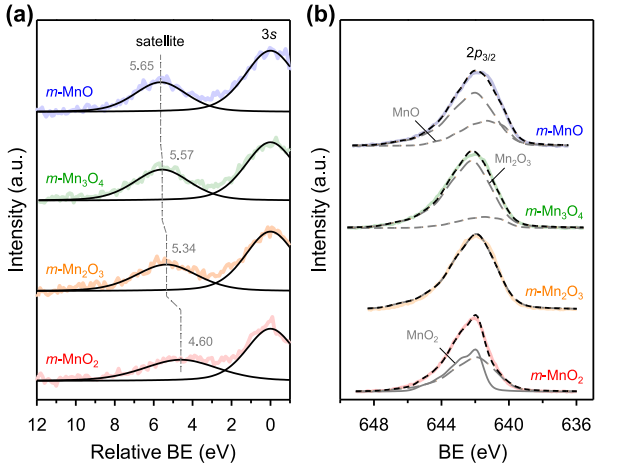

Figure 3. (a) Mn 3s XPS spectra of m-MnO_x where the Mn 3s main peaks are aligned to be 0 eV. The numbers indicate the splitting between the Mn 3s peak and its satellite peak. (b) Deconvoluted Mn $2p_{3/2}$ XPS spectra of m-MnO_x, considering complex multiplet splitting (see Figure S4).

S3).[8,53] The splitting value of 4.6 eV for m-MnO_2 is consistent with previously reported value for MnO_2.[8,53,54] The splitting values are larger for lower-valent MnO_x ranging from 5.3 eV for Mn_2O_3 to 6.0 eV for MnO.[8,53,54] The splitting values for m-Mn_2O_3 (5.34 eV) and m-Mn_3O_4 (5.57 eV) agree well with the previous results, although Mn_2O_3 and Mn_3O_4 are poorly resolved using this method due to large deviations of the splitting values, particularly for Mn_3O_4. The value of m-MnO (5.65 eV) suggests that this sample has an oxidized surface. Deconvolution of Mn 2p XPS spectra is complicated due to complex spectral phenomena in metal 2p transitions, which lead to multiplet splitting even in Mn compounds with a single Mn valence.[54,55] Nevertheless, complex multiplet peak fitting was attempted with the reference data previously reported.[55] In this method, each reference MnO_2, Mn_2O_3, and MnO Mn $2p_{3/2}$ XPS spectrum contains five multiplet peaks (Figures S4 and S5). The multiplet peak parameters were used to deconvolute the Mn $2p_{3/2}$ XPS spectra of m-MnO_x samples (Figure 3b and S4). These fitting results clearly show the difference between the samples, where the average surface oxidation states (ASOS) of m-MnO_2, m-Mn_2O_3, m-Mn_3O_4, and m-MnO are 3.5, 3.0, 2.9, and 2.7, respectively. A slight inconsistency in the ASOS of m-MnO_2 determined from 3s and $2p_{3/2}$ was found because the determination of ASOS using this method requires the standard XPS spectra of the reference samples taken from the instruments that we used. Despite this,

https://doi.org/10.1021/acsami.3c03358
ACS Appl. Mater. Interfaces 2023, 15, 31393–31402

the trends of these values are well consistent with what are expected from the bulk oxidation states.

XAS was used to study the bulk oxidation states and local structures of the catalysts. The X-ray absorption near edge structure (XANES) spectra of *m*-MnO_x and b-MnO_x are presented in Figure 4a. The XANES spectra of *m*-MnO_2, *m*-Mn_2O_3, and *m*-Mn_3O_4 overlapped with those of b-*β*-MnO_2, b-Mn_2O_3, and b-Mn_3O_4, respectively, indicating identical local structures and oxidation states. The slight disorder in *m*-MnO_2 (indicated by XRD analysis) was not prominent in the XANES spectra, possibly because the XANES spectra are sensitive to the first coordination-shell geometry. However, considerable differences were observed in the XANES spectra of *m*-MnO and b-MnO. Notably, the edge energy of *m*-MnO was higher than that of b-MnO, indicating a higher oxidation state of Mn in *m*-MnO. A linear graph representing the relationship between the edge energy and oxidation state was used to estimate the Mn valence in *m*-MnO (Figure 4b). The oxidation states of *m*-MnO_2, *m*-Mn_2O_3, and *m*-Mn_3O_4 were identified to be the same as their bulk counterparts, whereas the Mn valence of *m*-MnO is +2.36 ± 0.06. This could be attributed to the extensive surface oxidation of *m*-MnO due to its large surface area (71 $m^2\ g^{-1}$). Meanwhile, the oxidized layer was assumed to be very thin and/or amorphous since the oxidized phase was not detected by XRD.

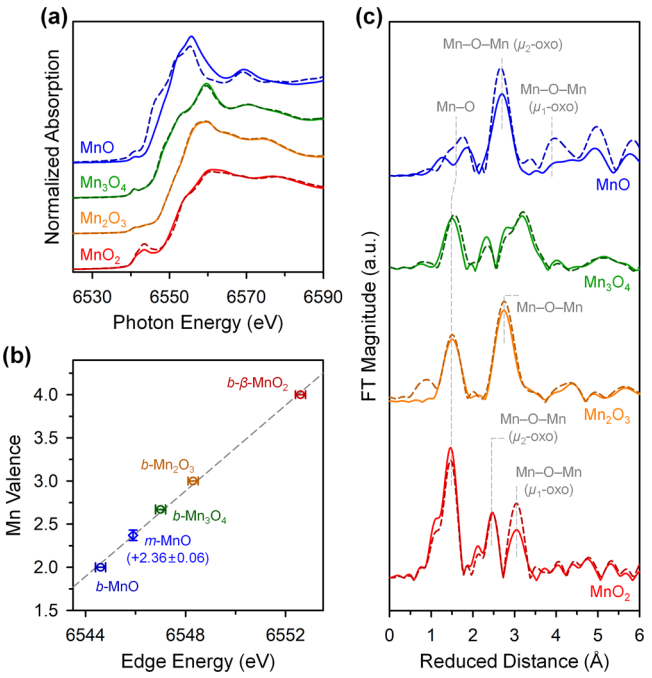

Figure 4. (a) Mn K-edge XANES spectra of *m*-MnO_x (solid lines) and b-MnO_x (dotted lines). (b) Linear relation between Mn valence and edge energy in the XANES spectra of the *m*-MnO and b-MnO_x, measured in the transmission mode. The data points for *m*-MnO_2, *m*-Mn_2O_3, and *m*-Mn_3O_4 are not shown, as they exhibit similar edge energies as their bulk counterparts. The error of the Mn valence was calculated to be 0.07, 0.06, and 0.06 for *m*-MnO_2, *m*-Mn_2O_3, and *m*-Mn_3O_4, respectively. (c) RDFs obtained from the k^3-weighted EXAFS spectra of *m*-MnO_x (bright-colored solid lines) and b-MnO_x (dark-colored dotted lines).

The local structure of *m*-MnO_x was investigated using EXAFS. The radial distribution functions (RDFs) of the k^3-weighted EXAFS spectra are shown in Figure 4c. The *m*-MnO_x catalysts showed unique structural characteristics analogous to those of the bulk MnO_x phases. All *m*-MnO_x show the main spectral peak at 1.5−1.6 Å corresponding to the Mn−O bond distance. The local structure of *m*-MnO_2 and *m*-Mn_2O_3 is similar in that they are composed of the mixed corner- and edge-shared MnO_6 octahedra, suggesting that both provide MnO_6-based active sites on their surfaces. However, the MnO_6 octahedra linkage structure critically impacts the electrocatalytic activity. For example, the Mn−O−Mn μ_2-oxo structure, found in the Mn_4O_4 cubane structure present in the natural Mn_4CaO_5 cluster, has been suggested as the active structure of MnO_x.[56,57] Such structures are found in edge-shared MnO_6 linkage structures.[22,38,40,43] Both *m*-MnO_2 and *m*-Mn_2O_3 contain the edge-shared MnO_6 octahedra, evidenced by the second EXAFS peaks at 2.4 Å for *m*-MnO_2 and 2.7 Å for *m*-Mn_2O_3 in their EXAFS spectra (Figure 4c). The higher Mn valence in *m*-MnO_2 results in a shorter Mn−O bond distance compared with that of *m*-Mn_2O_3.[58] For *m*-MnO_x, the next peak at 3.1 Å indicated the interatomic distance of μ_1-oxo-bridged Mn−O−Mn species found in corner-sharing MnO_6 (Figure 4c). The peak for the μ_1-oxo Mn species is smaller for *m*-MnO_2 compared with b-*β*-MnO_2, which is indicative of lacking a long-range order or slightly disordered structure of *m*-MnO_2 compared to b-*β*-MnO_2. MnO_x catalysts with a higher relative intensity of the second peak to the third peak showed better electrocatalytic activity for ORR and OER.[22,38,40,43] For the ORR, there have been a small number of publications so far regarding the local structure effect on the ORR activity. However, Mn cations in octahedral sites were suggested to be responsible for the high activity of Mn-based spinel oxides.[59] Hence, the structural features of *m*-MnO_2 and *m*-Mn_2O_3 can contribute to their high initial ORR and OER activity. Mn_3O_4 consists of $Mn^{2+}O_4$ tetrahedra and $Mn^{2+}O_6$ and $Mn^{3+}O_6$ octahedra structural units. MnO is composed of only corner-shared $Mn^{2+}O_6$ octahedra. The lower Mn oxidation states in those phases, combined with the poor structural requirement, are ascribed to the low oxygen electrocatalytic activities of *m*-Mn_3O_4 and *m*-MnO. However, the slight activity of *m*-Mn_3O_4 and *m*-MnO originates from the electrochemical phase transformation (or activated) into high-valent Mn species with μ_2-oxo conformation, which is, however, not efficient as Mn_2O_3 and MnO_2. In addition, *m*-MnO exhibited considerably lower Mn−Mn scattering intensity than b-MnO, which could be attributed to an atomic disorder in the oxidized surface layer of *m*-MnO. The slightly oxidized surface of *m*-MnO can benefit the electrocatalysis as demonstrated that MnO nanoparticles with oxidized surfaces generated active Mn(IV)═O species during the OER under a neutral condition.[33]

Electrocatalytic Performance. The materials characterization results indicate that the *m*-MnO_x catalysts have similar framework structures and textural properties but different chemical states and local structures. Hence, they can be used as model catalysts to investigate the effect of the oxidation states and local structures on electrocatalytic performances. The ORR and OER bifunctional activity of *m*-MnO_x was evaluated in an alkaline solution. Figure 5 shows the linear sweep voltammetry (LSV) curves of *m*-MnO_x, Vulcan carbon black, and commercial precious metal benchmark catalysts measured in O_2-saturated 0.1 M KOH. In general, *m*-MnO_x with a higher oxidation state showed better ORR activity. The *m*-MnO_2 and *m*-Mn_2O_3 exhibit the most positive onset potentials (0.84 and 0.87 V vs RHE, respectively) among the *m*-MnO_x catalysts. The ORR onset potential was defined arbitrarily as the

https://doi.org/10.1021/acsami.3c03358
ACS Appl. Mater. Interfaces 2023, 15, 31393−31402

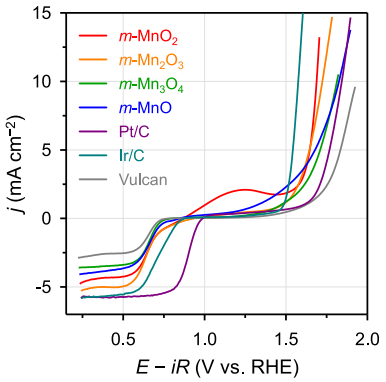

Figure 5. LSV curves simultaneously showing ORR and OER activities of *m*-MnO_x, Vulcan carbon black, Pt/C, and Ir/C, measured in an O_2-saturated 0.1 M KOH solution in the anodic direction, with an electrode rotation of 1600 rpm.

potential at a current density of −0.2 mA cm^{-2}. The onset potentials of *m*-MnO_2 and *m*-Mn_2O_3 were comparable to that of commercial Ir/C (0.84 V) and Pt/C (0.97 V). In contrast, *m*-Mn_3O_4 and *m*-MnO exhibited ORR onset potentials of 0.74 and 0.78 V (vs RHE), respectively. Magnified LSV curves clearly indicate the difference in activity between the catalysts (Figure S5). Comparing the diffusion-limited current density at higher overpotentials indicates the number of electrons transferred during the ORR, which is closely related to the efficiency of the reaction, according to the Levich equation.[14] Diffusion-limited current density trends are analogous to the ORR onset potentials of *m*-MnO_x catalysts. Consequently, the ORR activity of *m*-MnO_x catalysts increases in the following order: Mn_3O_4 < MnO < MnO_2 < Mn_2O_3. Interestingly, *m*-MnO exhibited better ORR activity than *m*-Mn_3O_4. This result is contradictory to previous reports, where MnO usually showed inferior ORR activity to any other MnO_x and even to glassy carbon electrodes.[14,17] The higher ORR activity of *m*-MnO compared to that of *m*-Mn_3O_4 is ascribed to the oxidized surface layer of the former with a disordered atomic arrangement. This is consistent with the previous reports demonstrating that surface oxidation could improve ORR activity.[33,60]

The OER activity of *m*-MnO_x catalysts increases in the following order: Mn_3O_4 ≈ MnO < MnO_2 ≈ Mn_2O_3. The potential at a current density of 10 mA cm^{-2} is generally used as a metric for the OER activity because of its relevance to the practical solar water splitting efficiency.[8] For reaching a current density of 10 mA cm^{-2}, overpotentials of 470, 490, 580, and 600 mV were required for *m*-MnO_2, *m*-Mn_2O_3, *m*-Mn_3O_4, and *m*-MnO, respectively (Table S2). For the OER, *m*-MnO_x with higher oxidation states exhibits better OER activity. For *m*-MnO_2, a broad bump centered at around 1.2 V was observed in the LSV plot; this could be attributed to the in situ oxidation peroxide species at the ORR potentials. For *m*-MnO, the oxidation current starts at ∼1.1 V (vs RHE), which originates from the oxidation of the catalyst itself. This phenomenon hindered a comparison of the OER activity. Thus, the OER activity was subsequently assessed separately and has been discussed in the following sections. The improvement of electrocatalytic activities that benefitted from the mesoporous structures was confirmed by measuring the ORR and OER activities of b-MnO_x (Figure S6). The ORR onset potentials were positively shifted by 10−100 mV, while the OER activity was improved by the factor of 1.8−2.6 in terms of the current density at 1.70 V (vs RHE) (Table S2). Mesopores could increase the electrochemically accessible area and facilitate mass transport, both of which improve the electrocatalytic activity. However, identifying the major contributor between the two factors is not a simple task and thus requires a systematic study. The OER activity improvement factor of 1.8−2.6 is insufficient and cannot be fully explained by the tens of times larger specific surface area of *m*-MnO_x than b-MnO_x. It is assumed that this could be ascribed to the phase-dependent electrical conductivity and different electrical contact between the electrode and the catalyst particles.

ORR Pathways. The number of electrons transferred during the ORR with *m*-MnO_x was investigated using rotating ring disk electrode (RRDE) (Figure 6a). The electron transfer

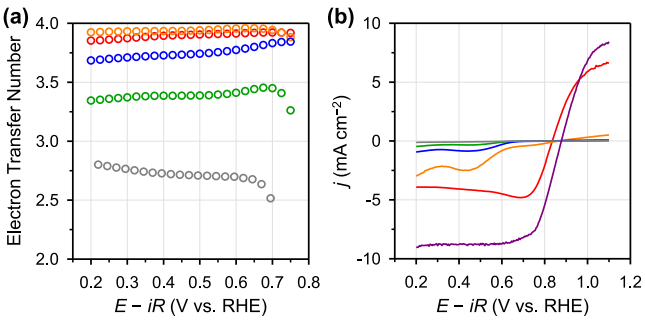

Figure 6. (a) Number of electrons transferred during the ORR measured by the RRDE method. (b) LSV curves in N_2-saturated 0.1 M KOH + 5 mM H_2O_2 at an electrode rotation speed of 1600 rpm to evaluate the electrochemical H_2O_2 oxidation/reduction activity. Measurements were performed immediately after the addition of H_2O_2 to N_2-saturated 0.1 M KOH to minimize the decomposition of H_2O_2 in the alkaline solution. Color code: red for *m*-MnO_2, orange for *m*-Mn_2O_3, green for *m*-Mn_3O_4, blue for *m*-MnO, gray for Vulcan, and magenta for Pt/C.

numbers of *m*-MnO_2 and *m*-Mn_2O_3 exceed 3.85 over the entire potential range investigated, indicating that they were the most efficient ORR catalysts among the samples. The maximum electron transfer number of *m*-Mn_2O_3 (3.96) was slightly higher than that for *m*-MnO_2 (3.92). Furthermore, the *m*-Mn_3O_4 and *m*-MnO catalysts have maximum electron transfer numbers of 3.45 and 3.84, respectively, where *m*-MnO showed a better reaction efficiency. The ORR 4-electron selectivity trends assessed by the RRDE method were consistent with the LSV results. The ORR selectivity of *m*-MnO_x was expressed as the OH_2^- (alkaline form of H_2O_2) production yield during the ORR because H_2O_2 is the 2-electron ORR product (Figure S7). Analyzing the reactivity of H_2O_2 with the different catalysts can provide mechanistic insights into the ORR pathway. For this purpose, the electrochemical H_2O_2 reduction was conducted in N_2-saturated 0.1 M KOH with 5 mM H_2O_2 (Figure 6b). In particular, *m*-MnO_2 exhibited high currents originating predominantly from the H_2O_2 redox reactions. The measurements performed using electrolytes with H_2O_2 concentrations in the range of 1.2−15 mM revealed that the redox current of *m*-MnO_2 was generated from the electrochemical reaction of H_2O_2 (Figure S8). The high H_2O_2 oxidation activity of *m*-MnO_2 could be the main reason for the current bump observed during LSV as the potential was scanned from the ORR to OER potentials (Figure 5). The other *m*-MnO_x catalysts did not show remarkable electrochemical responses for H_2O_2. Notably, the H_2O_2 reduction

https://doi.org/10.1021/acsami.3c03358
ACS Appl. Mater. Interfaces 2023, 15, 31393−31402

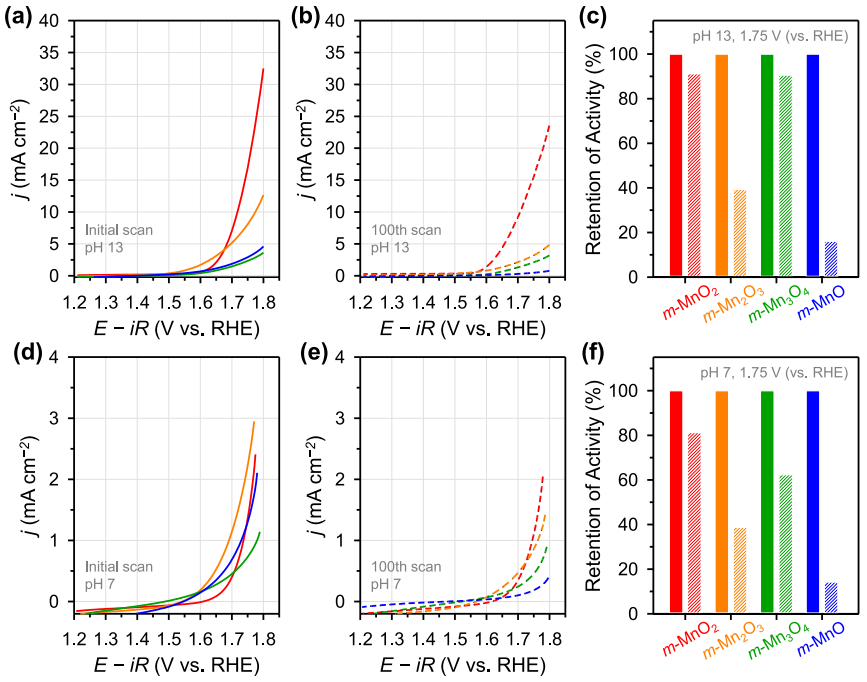

Figure 7. OER polarization curves obtained from the backward sweep of CV conducted at an electrode rotation speed of 1600 rpm. (a) Initial and (b) 100th scan measured in 0.1 M KOH. (c) Retention of the OER activity after 100 potential cycles in 0.1 M KOH. (d) Initial and (e) 100th scan measured in 0.1 M KPi buffer (pH 7). (f) Retention of the OER activity after 100 potential cycles in 0.1 M KPi buffer (pH 7). Color code: red for *m*-MnO_2, orange for *m*-Mn_2O_3, green for *m*-Mn_3O_4, and blue for *m*-MnO.

activity trends correlated well with the ORR activity and 4-electron selectivity for *m*-Mn_2O_3, *m*-Mn_3O_4, and *m*-MnO. This observation may suggest that *m*-MnO_2 took different ORR pathways compared to the other *m*-MnO_x catalysts. The similar ORR activity and 4-electron selectivity of *m*-Mn_2O_3 and *m*-MnO_2, despite the lower H_2O_2 reduction activity of *m*-Mn_2O_3, suggests that *m*-Mn_2O_3 catalyzes the ORR via a direct 4-electron pathway, indicating its higher intrinsic ORR activity than the other *m*-MnO_x. In contrast, for *m*-MnO_2, O_2 is first reduced to H_2O_2, which is then further reduced to H_2O inside the mesopores of *m*-MnO_2, completing the 4-electron ORR. This is also known as the 2 × 2-electron ORR pathway.[14] The higher ORR efficiency of *m*-MnO than *m*-Mn_3O_4 is attributed to the better H_2O_2 reduction activity of *m*-MnO.

OER Durability. As durability is a critical factor for practical application, the OER activity and durability of the *m*-MnO_x catalysts were assessed by cyclic voltammetry (CV) cycling in the OER potential range (Figure 7). The backward sweep is shown in Figure 7 because the forward sweep involves the current originating from the oxidation of the catalyst itself. Among all the catalysts analyzed, *m*-Mn_2O_3 showed the lowest onset potential (1.52 V vs RHE). The *m*-MnO_2 exhibited a slightly higher OER onset potential than *m*-Mn_2O_3 but a larger current density at high overpotentials. The *m*-Mn_3O_4 and *m*-MnO showed comparable OER activity, which is, however, lower than those of *m*-MnO_2 and *m*-Mn_2O_3 (Figure 7a). Although high-valent Mn, particularly Mn(III), appeared to facilitate OER, it was detrimental to long-term cycling tests. After 100 potential cycles, *m*-Mn_2O_3 and *m*-MnO lost their initial OER activity by 60 and 84%, respectively (Figure 7b,c). In contrast, the OER activities of *m*-MnO_2 and *m*-Mn_3O_4 changed negligibly after cycling, with deactivation rates of 8 and 9%, respectively. OER electrocatalysis under neutral conditions affords an environmentally benign method to produce hydrogen via water splitting. Thus, the OER activity and durability of *m*-MnO_x in 0.1 M KPi buffer (pH 7.0) were also tested (Figure 7d–f). All the *m*-MnO_x catalysts showed lower OER activities in the neutral electrolyte than in the alkaline electrolyte, possibly because of the lower concentration of reactant (H^+) in the former. The trends of the initial OER activity were similar in the neutral electrolyte, with marginal differences among the catalysts. The *m*-Mn_2O_3 exhibited the highest initial OER activity, with an onset overpotential of 370 mV. Although *m*-MnO_2 showed a slightly lower OER activity than *m*-Mn_2O_3 (with an onset overpotential is 440 mV), its current density increased steeply as the applied potential increased. This was similarly observed in the alkaline electrolyte. In spite of high initial activity, *m*-Mn_2O_3 shows a considerable loss of activity by 61%. In contrast, *m*-MnO_2 well maintained the initial activity, with 81% of the activity retained after 100 cycles. The OER activities of *m*-Mn_3O_4 and *m*-MnO were inferior to those of the other catalysts. Although *m*-MnO exhibited a slightly better initial OER activity than *m*-Mn_3O_4, its activity decreased dramatically by 86% after 100 potential cycles, whereas 62% of initial activity was maintained for *m*-Mn_3O_4. Speck et al. investigated the degradation mechanism of MnO_x during the OER using online inductively coupled plasma mass spectroscopy. Their study revealed that the dissolution rates of *β*-MnO_2 and Mn_2O_3 exhibited the same order of magnitude.[61] Thus, the faster activity decrease of *m*-Mn_2O_3 than *m*-MnO_2 could not be attributed to dissolution; the main degradation mechanism of *m*-Mn_2O_3 was assumed be the intrinsic instability of Mn(III) species, which easily undergoes disproportionation into Mn(II) and Mn(IV).[31] Therefore, considering both activity and durability in alkaline and neutral media, *m*-MnO_2 is the most suitable OER catalyst among all the *m*-MnO_x catalysts investigated. The retention of the OER activity

https://doi.org/10.1021/acsami.3c03358
ACS Appl. Mater. Interfaces 2023, 15, 31393−31402

of m-Mn_3O_4 after the OER cycles at pH 7 is slightly lower than that at pH 13. This is attributed to the pH-dependent mechanistic difference. Mn(III) disproportionation was suggested to be related to the degradation of MnO_x-based OER catalysts.[31] Mn dissolution can also contribute to the decline of the OER activity. The dissolved species might be re-deposited into $Mn(OH)_x$ species, which could then be involved again in the electrocatalysis. The re-deposition of oxide-based OER electrocatalysts is a well-accepted catalyst recovery mechanism.[62] The deactivation percentages of 8−9 and 14−19% in the alkaline and neutral electrolytes are significant in practical applications where thousand-hours stability must be guaranteed. However, since many parameters other than the chemical states and structures of electrocatalysts affect the stability, the improvement of stability requires further research, including fine-tuning the catalyst structure as well as controlling some variables in the electrode fabrication such as catalyst ink composition, drying conditions, type of electrode substrate, and deposition methods.

The β-MnO_2 phase usually exhibited mediocre ORR and OER activities compared to the other MnO_x phases.[37,44,63,64] This has been elucidated by a narrow $[1 \times 1]$ tunnel structure composed of corner-sharing MnO_6 octahedra in the β-MnO_2 phase. The empty space within such a compact structure is extremely small and thus is insufficient for the accommodation of even water molecules. The poor active-site accessibility, owing to a narrow tunnel structure, limits the oxygen electrocatalytic activity of β-MnO_2. However, m-MnO_2, which consists of irregularly linked MnO_6 octahedra, shows ORR and OER bifunctional activity comparable to that of m-Mn_2O_3. The excellent catalytic performance of m-MnO_2 can be attributed to the disorder in the atomic arrangement, as well as the presence of mesopores channels that facilitate mass transport. These factors also increase the accessibility of the reactants to the active μ_2-oxo Mn sites of the catalyst.

In Situ XANES Analysis. To identify changes in the structure and oxidation state during the electrocatalysis, in situ XAS experiments were conducted in 0.1 M KOH under different applied potentials (Figure 8). XAS spectra were first obtained without an applied potential, then at 0.6 V (vs RHE) and 1.8 V (vs RHE), where ORR and OER occur, respectively. A slight increase in the white-line intensity was observed for all catalysts under the ORR and OER potentials. This indicates additional Mn−O bonding between oxygen-related intermediates (e.g., O, OH, and OOH) and Mn during the ORR and OER, suggesting the involvement of m-MnO_x in oxygen electrocatalysis regardless of the local structure and oxidation state. However, the increased intensity is not related to the activity improvement factor. Using the Mn valence-edge energy correlation obtained in the fluorescence detection mode (Figure S9), the oxidation states of m-MnO_2, m-Mn_2O_3, m-Mn_3O_4, and m-MnO were found to be 4.03, 3.05, 2.71, and 2.56 ± 0.10 under the fresh conditions (in the electrolyte without the applied potential, Table S3). These values are similar to their ex situ XANES results (Figure 4a), except that m-MnO showed a slightly more oxidized state, presumably originating from electrolyte-induced oxidation. At the ORR potential, m-Mn_2O_3, m-Mn_3O_4, and m-MnO maintained their initial oxidation states, indicating the Mn valences of +2 and +3 are thermodynamically stable under the ORR conditions. In contrast, m-MnO_2 was reduced at the ORR potential with the resulting oxidation state of 3.78 ± 0.10, which was considerably lower than 4.03 ± 0.10 at the fresh conditions.

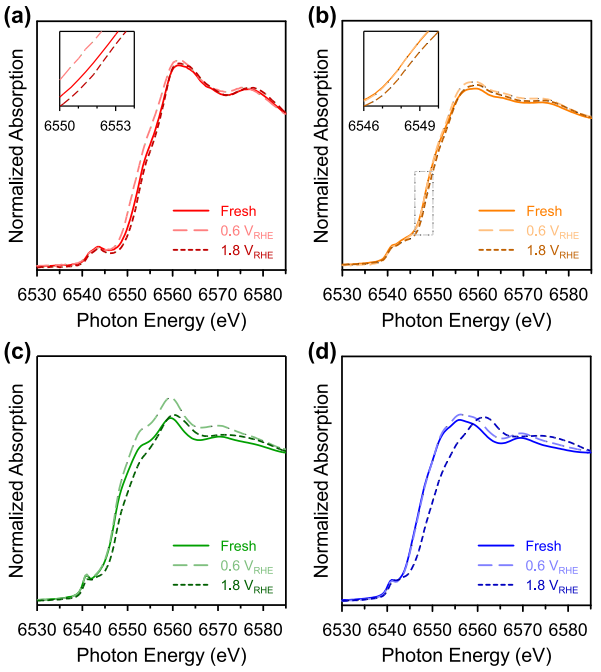

Figure 8. In situ XANES spectra of (a) m-MnO_2, (b) m-Mn_2O_3, (c) m-Mn_3O_4, and (d) m-MnO acquired in 0.1 M KOH without an applied potential (denoted as fresh) and with applied potentials at 0.6 and 1.8 V (vs RHE), where ORR and OER occur, respectively. For m-MnO_2 and m-Mn_2O_3, magnified XANES spectra are also shown as the inset figure. Color code: red for m-MnO_2, orange for m-Mn_2O_3, green for m-Mn_3O_4, and blue for m-MnO.

These results imply the generation and participation of Mn(III) species in the ORR. When the OER potential was applied, all m-MnO_x catalysts showed increases in the Mn oxidation states to different extents, depending on the catalyst (by 0.1−0.4, Table S3). The m-Mn_2O_3 exhibited more oxidized states compared to its fresh state, with the oxidation state being 3.15 ± 0.10. m-Mn_3O_4 and m-MnO also showed higher Mn valences under the OER conditions than the fresh conditions, with the Mn oxidation states of 2.95 and 2.86 ± 0.10, respectively. Because the XANES is a bulk-averaging characterization technique, the change of the surface oxidation state is typically not well observed in the in situ XANES spectra. In this regard, m-Mn_2O_3 and m-Mn_3O_4 showed a small increase of the Mn oxidation states by 0.10 and 0.15, respectively, at the OER potential, suggesting that the surface-limited phase transformation occurred for these catalysts. In contrast, m-MnO exhibited a large increase in the Mn oxidation state by ∼0.4. These results originate from the phase transformation occurring not only at the catalyst surface but also in their MnO_x framework cores into the thermodynamically favorable phases (which are oxidized forms). In situ XANES results of m-Mn_2O_3 and m-MnO_2 suggest the involvement of Mn(III)/Mn(IV) redox or Mn(V) intermediates during the OER.[65] Moreover, the in situ XANES results suggested that Mn(II) species hardly participate in both oxygen electrocatalysis.

The participation of Mn(III)/Mn(IV) redox in the OER has been suggested by several previous studies. Kaiser and co-workers performed the XPS analysis and showed that the MnO_x samples with Mn(IV) species possessed lower valence Mn species after the OER cycling, which could be ascribed to regeneration of active Mn(III) species.[66] The authors

https://doi.org/10.1021/acsami.3c03358
ACS Appl. Mater. Interfaces 2023, 15, 31393−31402

demonstrated operando Raman analysis with MnO_x films with controlled Mn oxidation states. They showed the co-existence of Mn(III) and Mn(IV) species at the OER potentials regardless of the initial oxidation state yet with different ratio. The reduction of initial Mn(IV) into Mn(III) states was also confirmed by the post XPS analysis by Speck et al.[61] Jaramillo and co-workers prepared MnO_x samples mainly consisting of Mn_2O_3 with a small amount of MnO. After the OER tests, the as-prepared MnO_x was transformed into $Mn^{III,IV}O_x$, with the initial MnO phase disappearing.[41] van de Krol and co-workers found that amorphous MnO_x films with the initial oxidation state of ~2 transformed into $Mn^{III,IV}O_x$ species as revealed by post XPS analysis.[67]

CONCLUSIONS

In summary, four types of ordered mesoporous manganese oxides with similar textural properties but different oxidation states and local structures were synthesized and tested as bifunctional electrocatalysts for the ORR and OER. The following electrocatalytic activity trends were obtained: *m*-Mn_2O_3 > *m*-MnO_2 > *m*-MnO > *m*-Mn_3O_4 for the ORR and *m*-MnO_2 > *m*-Mn_2O_3 > *m*-MnO ≈ *m*-Mn_3O_4 for the OER. *m*-MnO_2, mainly composed of β-MnO_2 which has been shown only mediocre activity for the ORR and OER, exhibited substantially high ORR activity, 4-electron selectivity, and OER activity. The high electrocatalytic activities of *m*-MnO_2 are attributed to the disordered arrangement of MnO_6 octahedra in *m*-MnO_2, which was induced by nanostructuring. Interestingly, *m*-MnO showed better electrocatalytic activity than *m*-Mn_3O_4, which is contradictory to the previous reports, which demonstrated low electrocatalytic activity of MnO. This could be ascribed to the oxidized surface of the *m*-MnO catalyst, combined with the high surface area, leading to the extensive formation of surface Mn(III) species. The activity trends revealed the importance of higher-valent Mn (Mn(III) and Mn(IV)) for oxygen electrocatalysis, whereas Mn(II) species played a negligible role. Finally, the changes in the oxidation state during oxygen electrocatalysis were investigated using in situ XANES that indicated the generation of Mn(III) and Mn(IV) species and the participation of such species in electrocatalytic reactions. This study provides guidelines for the development of advanced Mn-based bifunctional oxygen electrocatalysts.

ASSOCIATED CONTENT

Supporting Information

The Supporting Information is available free of charge at https://pubs.acs.org/doi/10.1021/acsami.3c03358.

Additional experimental details; textural properties of *m*-MnO_x; SEM images of *m*-MnO_x; deconvoluted Mn $2p_{3/2}$ XPS spectra of *m*-MnO_x; Mn 3s XPS spectra of b-MnO_x; magnified ORR LSV curves; ORR and OER activities of b-MnO_x; H_2O_2 selectivity of *m*-MnO_x; electrochemical H_2O_2 redox activity of *m*-MnO_2; edge energy-valence relationship in fluorescence detection mode; and XRD pattern of b-β-MnO_2 (PDF)

AUTHOR INFORMATION

Corresponding Authors

Young Jin Sa − *Department of Chemistry, Kwangwoon University, Seoul 01897, Republic of Korea;* orcid.org/0000-0003-4579-0491; Email: youngjinsa@kw.ac.kr

Sang Hoon Joo − *Department of Chemistry, Seoul National University, Seoul 08826, Republic of Korea;* orcid.org/0000-0002-8941-9662; Email: shjoo1@snu.ac.kr

Authors

Sohee Kim − *Department of Chemistry, Kwangwoon University, Seoul 01897, Republic of Korea*

Yesol Lee − *Department of Chemistry, Kwangwoon University, Seoul 01897, Republic of Korea*

Ji Man Kim − *Department of Chemistry, Sungkyunkwan University, Suwon 16419, Republic of Korea;* orcid.org/0000-0003-0860-4880

Complete contact information is available at: https://pubs.acs.org/10.1021/acsami.3c03358

Notes

The authors declare no competing financial interest.

ACKNOWLEDGMENTS

S.H.J. were supported by the National Research Foundation (NRF) of Korea, funded by the Ministry of Science and ICT (NRF-2021R1A2C2007495). This present research has been conducted by the Excellent researcher support project of Kwangwoon University in 2021. The XAS experiments performed at the Beamline 10C of Pohang Accelerator Laboratory (PAL) were supported in part by MSIT and POSTECH. We thank Dr. Du San Baek for his artwork in the paper.

REFERENCES

(1) Park, S.; Shao, Y.; Liu, J.; Wang, Y. Oxygen Electrocatalysts for Water Electrolyzers and Reversible Fuel Cells: Status and Perspective. *Energy Environ. Sci.* **2012**, *5*, 9331−9334.

(2) Bruce, P. G.; Freunberger, S. A.; Hardwick, L. J.; Tarascon, J.-M. $Li-O_2$ and Li−S Batteries with High Energy Storage. *Nat. Mater.* **2012**, *11*, 19−29.

(3) Katsounaros, I.; Cherevko, S.; Zeradjanin, A. R.; Mayrhofer, K. J. J. Oxygen Electrochemistry as a Cornerstone for Sustainable Energy Conversion. *Angew. Chem., Int. Ed.* **2014**, *53*, 102−121.

(4) Jiao, Y.; Zheng, Y.; Jaroniec, M.; Qiao, S. Z. Design of Electrocatalysts for Oxygen- and Hydrogen-Involving Energy Conversion Reactions. *Chem. Soc. Rev.* **2015**, *44*, 2060−2086.

(5) Cheng, F.; Chen, J. Metal-Air Batteries: from Oxygen Reduction Electrochemistry to Cathode Catalysts. *Chem. Soc. Rev.* **2012**, *41*, 2172−2192.

(6) Gasteiger, H. A.; Kocha, S. S.; Sompalli, B.; Wagner, F. T. Activity Benchmarks and Requirements for Pt, Pt-Alloy, and Non-Pt Oxygen Reduction Catalysts for PEMFCs. *Appl. Catal., B* **2005**, *56*, 9−35.

(7) Chen, G.; Bare, S. R.; Mallouk, T. E. Development of Supported Bifunctional Electrocatalysts for Unitized Regenerative Fuel Cells. *J. Electrochem. Soc.* **2002**, *149*, A1092−A1099.

(8) Gorlin, Y.; Jaramillo, T. F. A Bifunctional Nonprecious Metal Catalyst for Oxygen Reduction and Water Oxidation. *J. Am. Chem. Soc.* **2010**, *132*, 13612−13614.

(9) Valim, R. B.; Santos, M. C.; Lanza, M. R. V.; Machado, S. A. S.; Lima, F. H. B.; Calegaro, M. L. Oxygen Reduction Reaction Catalyzed by ε-MnO_2: Influence of the Crystalline Structure on the Reaction Mechanism. *Electrochim. Acta* **2012**, *85*, 423−431.

(10) El-Sawy, A. M.; King'ondu, C. K.; Kuo, C.-H.; Kriz, D. A.; Guild, C. J.; Meng, Y.; Frueh, S. J.; Dharmarathna, S.; Ehrlich, S. N.; Suib, S. L. X-ray Absorption Spectroscopic Study of a Highly Thermally Stable Manganese Oxide Octahedral Molecular Sieve (OMS-2) with High Oxygen Reduction Reaction Activity. *Chem. Mater.* **2014**, *26*, 5752−5760.

(11) Zhao, Q.; Yan, Z.; Chen, C.; Chen, J. Spinels: Controlled Preparation, Oxygen Reduction/Evolution Reaction Application, and Beyond. *Chem. Rev.* **2017**, *117*, 10121−10211.
(12) Kuo, C.-H.; Mosa, I. M.; Poyraz, A. S.; Biswas, S.; El-Sawy, A. M.; Song, W.; Luo, Z.; Chen, S.-Y.; Rusling, J. F.; He, J.; Suib, S. L. Robust Mesoporous Manganese Oxide Catalysts for Water Oxidation. *ACS Catal.* **2015**, *5*, 1693−1699.
(13) Feng, J.; Liang, Y.; Wang, H.; Li, Y.; Zhang, B.; Zhou, J.; Wang, J.; Regier, T.; Dai, H. Engineering Manganese Oxide/Nanocarbon Hybrid Materials for Oxygen Reduction Electrocatalysis. *Nano Res.* **2012**, *5*, 718−725.
(14) Gorlin, Y.; Chung, C.-J.; Nordlund, D.; Clemens, B. M.; Jaramillo, T. F. Mn_3O_4 Supported on Glassy Carbon: An Active Non-Precious Metal Catalyst for the Oxygen Reduction Reaction. *ACS Catal.* **2012**, *2*, 2687−2694.
(15) Duan, J.; Zheng, Y.; Chen, S.; Tang, Y.; Jaroniec, M.; Qiao, S. Mesoporous Hybrid Material Composed of Mn_3O_4 Nanoparticles on Nitrogen-Doped Graphene for Highly Efficient Oxygen Reduction Reaction. *Chem. Commun.* **2013**, *49*, 7705−7707.
(16) Turekian, K. K.; Wedepohl, K. H. Distribution of the Elements in Some Major Units of the Earth's Crust. *Geol. Soc. Am. Bull.* **1961**, *72*, 175−192.
(17) Pickrahn, K. L.; Park, S. W.; Gorlin, Y.; Lee, H.-B.-R.; Jaramillo, T. F.; Bent, S. F. Active MnO_x Electrocatalysts Prepared by Atomic Layer Deposition for Oxygen Evolution and Oxygen Reduction Reactions. *Adv. Energy Mater.* **2012**, *2*, 1269−1277.
(18) Indra, A.; Menezes, P. W.; Zaharieva, I.; Baktash, E.; Pfrommer, J.; Schwarze, M.; Dau, H.; Driess, M. Active Mixed-Valent MnO_x Water Oxidation Catalysts through Partial Oxidation (Corrosion) of Nanostructured MnO Particles. *Angew. Chem., Int. Ed.* **2013**, *52*, 13206−13210.
(19) Zhuang, Q.; Ma, N.; Yin, Z.; Yang, X.; Yin, Z.; Gao, J.; Xu, Y.; Gao, Z.; Wang, H.; Kang, J.; Xiao, D.; Li, J.; Li, X.; Ma, D. Rich Surface Oxygen Vacancies of MnO_2 for Enhancing Electrocatalytic Oxygen Reduction and Oxygen Evolution Reactions. *Adv. Energy Sustainability Res.* **2021**, *2*, No. 2100030.
(20) Gorlin, Y.; Chung, C.-J.; Benck, J. D.; Nordlund, D.; Seitz, L.; Weng, T.-C.; Sokaras, D.; Clemens, B. M.; Jaramillo, T. F. Understanding Interactions between Manganese Oxide and Gold That Lead to Enhanced Activity for Electrocatalytic Water Oxidation. *J. Am. Chem. Soc.* **2014**, *136*, 4920−4926.
(21) Lee, J. H.; Sa, Y. J.; Kim, T. K.; Moon, H. R.; Joo, S. H. A Transformative Route to Nanoporous Manganese Oxides of Controlled Oxidation States with Identical Textural Properties. *J. Mater. Chem. A* **2014**, *2*, 10435−10443.
(22) Park, S.-A.; Lim, H.; Kim, Y.-T. Enhanced Oxygen Reduction Reaction Activity Due to Electronic Effect between Ag and Mn_3O_4 in Alkaline Media. *ACS Catal.* **2015**, *5*, 3995−4002.
(23) Mao, L.; Sotomura, T.; Nakatsu, K.; Koshiba, N.; Zhang, D.; Ohsaka, T. Electrochemical Characterization of Catalytic Activities of Manganese Oxides to Oxygen Reduction in Alkaline Aqueous Solution. *J. Electrochem. Soc.* **2002**, *149*, A504−A507.
(24) Lima, F. H. B.; Calegaro, M. L.; Ticianelli, E. A. Electrocatalytic Activity of Manganese Oxides Prepared by Thermal Decomposition for Oxygen Reduction. *Electrochim. Acta* **2007**, *52*, 3732−3738.
(25) Tang, Q.; Jiang, L.; Liu, J.; Wang, S.; Sun, Q. Effect of Surface Manganese Valence of Manganese Oxides on the Activity of the Oxygen Reduction Reaction in Alkaline Media. *ACS Catal.* **2014**, *4*, 457−463.
(26) Yano, J.; Yachandra, V. Mn_4Ca Cluster in Photosynthesis: Where and How Water is Oxidized to Dioxygen. *Chem. Rev.* **2014**, *114*, 4175−4205.
(27) Najafpour, M. M.; Ehrenberg, T.; Weichen, M.; Kurz, P. Calcium Manganese(III) Oxides ($CaMn_2O_4{\cdot}xH_2O$) as Biomimetic Oxygen-Evolving Catalysts. *Angew. Chem., Int. Ed.* **2010**, *49*, 2233−2237.
(28) Han, X.; Zhang, T.; Du, J.; Cheng, F.; Chen, J. Porous Calcium-Manganese Oxide Microspheres for Electrocatalytic Oxygen Reduction with High Activity. *Chem. Sci.* **2013**, *4*, 368−376.
(29) Al-Oweini, R.; Sartorel, A.; Bassil, B. S.; Natali, M.; Berardi, S.; Scandola, F.; Kortz, U.; Bonchio, M. Photocatalytic Water Oxidation by Mixed-Valent $Mn^{III}_3Mn^{IV}O_3$ Manganese Oxo Core that Mimics the Natural Oxygen-Evolving Center. *Angew. Chem., Int. Ed.* **2014**, *53*, 11182−11185.
(30) Kanady, J. S.; Tsui, E. Y.; Day, M. W.; Agapie, T. A Synthetic Model of the Mn_3Ca Subsite of the Oxygen-Evolving Complex in Photosystem II. *Science* **2011**, *333*, 733−736.
(31) Takashima, T.; Hashimoto, K.; Nakamura, R. Mechanisms of pH-Dependent Activity for Water Oxidation to Molecular Oxygen by MnO_2 Electrocatalysts. *J. Am. Chem. Soc.* **2012**, *134*, 1519−1527.
(32) Indra, A.; Menezes, P. W.; Schuster, F.; Driess, M. Significant Role of Mn(III) Sites in eg1 Configuration in Manganese Oxide Catalysts for Efficient Artificial Water Oxidation. *J. Photochem. Photobiol., B* **2015**, *152*, 156−161.
(33) Jin, K.; Seo, H.; Hayashi, T.; Balamurugan, M.; Jeong, D.; Go, Y. K.; Hong, J. S.; Cho, K. H.; Kakizaki, H.; Bonnet-Mercier, N.; Kim, M. G.; Nakamura, R.; Nam, K. T. Mechanistic Investigation of Water Oxidation Catalyzed by Uniform, Assembled MnO Nanoparticles. *J. Am. Chem. Soc.* **2017**, *139*, 2277−2285.
(34) Kok, B.; Forbush, B.; McGloin, M. Coorperation of Charges in Photosynthetic O_2 Evolution-I. A Linear Four Step Mechanism. *Photochem. Photobiol.* **1970**, *11*, 457−475.
(35) Cheng, F.; Zhang, T.; Zhang, Y.; Du, J.; Han, X.; Chen, J. Enhancing Electrocatalytic Oxygen Reduction on MnO_2 with Vacancies. *Angew. Chem., Int. Ed.* **2013**, *52*, 2474−2477.
(36) Kim, J.; Yin, X.; Tsao, K.-C.; Fang, S.; Yang, H. $Ca_2Mn_2O_5$ as Oxygen-Deficient Perovskite Electrocatalyst for Oxygen Evolution Reaction. *J. Am. Chem. Soc.* **2014**, *136*, 14646−14649.
(37) Robinson, D. M.; Go, Y. B.; Mui, M.; Gardner, G.; Zhang, Z.; Mastrogiovanni, D.; Garfunkel, E.; Li, J.; Greenblatt, M.; Dismukes, G. C. Photochemical Water Oxidation by Crystalline Polymorphs of Manganese Oxides: Structural Requirements for Catalysis. *J. Am. Chem. Soc.* **2013**, *135*, 3494−3501.
(38) Bergmann, A.; Zaharieva, I.; Dau, H.; Strasser, P. Electrochemical Water Splitting by Layered and 3D Crosslinked Manganese Oxides: Correlating Structural Motifs and Catalytic Activity. *Energy Environ. Sci.* **2013**, *6*, 2745−2755.
(39) Boppana, V. B. R.; Yusuf, S.; Hutchings, G. S.; Jiao, F. Nanostructured Alkaline-Cation-Containing δ-MnO_2 for Photocatalytic Water Oxidation. *Adv. Funct. Mater.* **2013**, *23*, 878−884.
(40) Najafpour, M. M.; Moghaddam, A. N.; Dau, H.; Zaharieva, I. Fragments of Layered Manganese Oxide are the Real Water-Oxidation Catalyst after Transformation of Molecular Precursor on Clay. *J. Am. Chem. Soc.* **2014**, *136*, 7245−7248.
(41) Gorlin, Y.; Lassalle-Kaiser, B.; Benck, J. D.; Gul, S.; Webb, S. M.; Yachandra, V. K.; Yano, J.; Jaramillo, T. F. In Situ X-ray Absorption Spectroscopy Investigation of a Bifunctional Manganese Oxide Catalyst with High Activity for Electrochemical Water Oxidation and Oxygen Reduction. *J. Am. Chem. Soc.* **2013**, *135*, 8525−8534.
(42) Jin, K.; Park, J.; Lee, J.; Yang, K. D.; Pradhan, G. K.; Sim, U.; Jeong, D.; Jang, H. L.; Park, S.; Kim, D.; Sung, N.-E.; Kim, S. H.; Han, S.; Nam, K. T. Hydrated Manganese(II) Phosphate ($Mn_3(PO_4)_2{\cdot}3H_2O$) as a Water Oxidation Catalyst. *J. Am. Chem. Soc.* **2014**, *136*, 7435−7443.
(43) Zaharieva, I.; Chernev, P.; Risch, M.; Klingan, K.; Kohlhoff, M.; Fischer, A.; Dau, H. Electrosynthesis, Functional, and Structural Characterization of a Water-Oxidizing Manganese Oxide. *Energy Environ. Sci.* **2012**, *5*, 7081−7089.
(44) Meng, Y.; Song, W.; Huang, H.; Ren, Z.; Chen, S.-Y.; Suib, S. L. Structure-Property Relationship of Bifunctional MnO_2 Nanostructures: Highly Efficient, Ultra-Stable Electrochemical Water Oxidation and Oxygen Reduction Reaction Catalysts Identified in Alkaline Media. *J. Am. Chem. Soc.* **2014**, *136*, 11452−11464.
(45) Cheng, F.; Su, Y.; Liang, J.; Tao, Z.; Chen, J. MnO_2-Based Nanostructures as Catalysts for Electrochemical Oxygen Reduction in Alkaline Media. *Chem. Mater.* **2010**, *22*, 898−905.

https://doi.org/10.1021/acsami.3c03358
ACS Appl. Mater. Interfaces 2023, 15, 31393−31402

(46) Kuo, C.-H.; Mosa, I. M.; Thanneeru, S.; Sharma, V.; Zhang, L.; Biswas, S.; Aindow, M.; Alpay, S. P.; Rusling, J. F.; Suib, S. L.; He, J. Facet-Dependent Catalytic Activity of MnO Electrocatalysts for Oxygen Reduction and Oxygen Evolution Reactions. *Chem. Commun.* **2015**, *51*, 5951−5954.
(47) Liu, J.; Jiang, L.; Zhang, T.; Jin, J.; Yuan, L.; Sun, G. Activating Mn_3O_4 by Morphology Tailoring for Oxygen Reduction. *Electrochim. Acta* **2016**, *205*, 38−44.
(48) Kim, T.-W.; Kleitz, B.; Paul, B.; Ryoo, R. MCM-48-like Large Mesoporous Silicas with Tailored Pore Structure: Facile Synthesis Domain in a Ternary Triblock Copolymer-Butanol-Water System. *J. Am. Chem. Soc.* **2005**, *127*, 7601−7610.
(49) Park, G. O.; Shon, J. K.; Kim, Y. H.; Kim, J. M. Synthesis of Ordered Mesoporous Manganese Oxides with Various Oxidation States. *J. Nanosci. Nanotechnol.* **2015**, *15*, 2441−2445.
(50) Ravel, B.; Newville, M. ATHENA, ARTEMIS, HEPHAESTUS: Data Analysis for X-Ray Absorption Spectroscopy Using IFEFFIT. *J. Synchrotron Radiat.* **2005**, *12*, 537−541.
(51) Albering, J. H. Structural Chemistry of Manganese Dioxide and Related Compounds. In *Handbook of Battery Materials*, 2nd edition; Daniel, C.; Besenhard, J. O., Eds.; Wiley-VCH: Verlag GmbH & Co. KGaA: Weinheim, 2011; pp 89−123.
(52) Jiao, F.; Hill, A. H.; Harrison, A.; Berko, A.; Chadwick, A. V.; Bruce, P. G. Synthesis of Ordered Mesoporous NiO with Crystalline Walls and a Bimodal Pore Size Distribution. *J. Am. Chem. Soc.* **2008**, *130*, 5262−5266.
(53) Ilton, E. S.; Post, J. E.; Heaney, P. J.; Ling, F. T.; Kerisit, S. N. XPS Determination of Mn Oxidation states in Mn (hydro)xides. *Appl. Surf. Sci.* **2016**, *366*, 475−485.
(54) Hyunh, M.; Shi, C.; Billinge, S. J. L.; Nocera, D. G. Nature of Activated Manganese Oxide for Oxygen Evolution. *J. Am. Chem. Soc.* **2015**, *137*, 14887−14904.
(55) Biesinger, M. C.; Payne, B. P.; Grosvenor, A. P.; Lau, L. W. M.; Gerson, A. R.; Smart, R. C. Resolving Surface Chemical States in XPS Analysis of First Row Transition Metals, Oxides and Hydroxides: Cr, Mn, Fe, Co and Ni. *Appl. Surf. Sci.* **2011**, *257*, 2717−2730.
(56) Smith, P. F.; Deibert, B. J.; Kaushik, S.; Gardner, G.; Hwang, S.; Wang, H.; Al-Sharab, J. F.; Garfunkel, E.; Fabris, L.; Li, J.; Dismukes, G. C. Coordination Geometry and Oxidation State Requirements of Corner-Sharing MnO_6 Octahedra for Water Oxidation Catalysis: An Investigation of Manganite (γ-MnOOH). *ACS Catal.* **2016**, *6*, 2089−2099.
(57) Zaharieva, I.; González-Flores, D.; Asfari, B.; Pasquini, C.; Mohammadi, M. R.; Klingan, K.; Zizak, I.; Loos, S.; Chernev, P.; Dau, H. Water Oxidation Catalysis — Role of Redox and Structural Dynamics in Biological Photosynthesis and Inorganic Manganese Oxides. *Energy Enrivon. Sci.* **2016**, *9*, 2433−2443.
(58) Bernardini, S.; Bellatreccia, F.; Della Ventura, G.; Sodo, A. A Reliable Method for Determining the Oxidation State of Manganese at the Microscale in Mn Oxides *via* Raman Spectroscopy. *Geostand. Geoanal. Res.* **2020**, *45*, 223−244.
(59) Kim, J.; Ko, W.; Yoo, J. M.; Paidi, V. K.; Jang, H. Y.; Shepit, M.; Lee, J.; Chang, H.; Lee, H. S.; Jo, J.; Kim, B. H.; Cho, S.-P.; van Lierop, J.; Kim, D.; Lee, K.-S.; Back, S.; Sung, Y.-E.; Hyeon, T. Structural Insights into Multi-Metal Spinel Oxide Nanoparticles for Boosting Oxygen Reduction Electrocatalysis. *Adv. Mater.* **2022**, *34*, No. 2107868.
(60) He, S.; Ji, D.; Novello, P.; Li, X.; Liu, J. Partial Surface Oxidation of Manganese Oxides as an Effective Treatment to Improve Their Activity in Electrochemical Oxygen Reduction Reaction. *J. Phys. Chem. C* **2018**, *122*, 21366−21374.
(61) Speck, F. D.; Santori, P. G.; Jaouen, F.; Cherevko, S. Mechanisms of Manganese Oxide Electrocatalysts Degradation during Oxygen Reduction and Oxygen Evolution Reactions. *J. Phys. Chem. C* **2019**, *123*, 25267−25277.
(62) Fabbri, E.; Schmidt, T. J. Oxygen Evolution Reaction—The Enigma in Water Electrolysis. *ACS Catal.* **2018**, *8*, 9765−9774.
(63) Lima, F. H. B.; Calegaro, M. L.; Ticianelli, E. A. Investigations of the Catalytic Properties of Manganese Oxides for the Oxygen Reduction in Alkaline Media. *J. Electroanal. Chem.* **2006**, *590*, 152−160.
(64) Cao, Y. L.; Yang, H. X.; Ai, X. P.; Xiao, L. F. The Mechanism of Oxygen Reduction on MnO_2-Catalyzed Air Cathode in Alkaline Solution. *J. Electroanal. Chem.* **2003**, *557*, 127−134.
(65) Roy, I.; Wang, Q.; Chakrapani, V. Nature of Reaction Intermediates and Origin of Bifunctionality in Manganese Oxide. *J. Phys. Chem. C* **2020**, *124*, 5286−5299.
(66) Radinger, H.; Connor, P.; Stark, R.; Jaegermann, W.; Kaiser, B. Manganese Oxide as an Inorganic Catalyst for the Oxygen Evolution Reaction Studied by X-Ray Photoelectron and Operando Raman Spectroscopy. *ChemCatChem* **2021**, *13*, 1175−1185.
(67) Plate, P.; Höhn, C.; Bloeck, U.; Bogdanoff, P.; Fiechter, S.; Abdi, F. F.; van de Krol, R.; Bronneberg, A. C. On the Origin of the OER Activity of Ultrathin Manganese Oxide Films. *ACS Appl. Mater. Interfaces* **2021**, *13*, 2428−2436.

https://doi.org/10.1021/acsami.3c03358
ACS Appl. Mater. Interfaces 2023, 15, 31393−31402